Received Date : 13-Nov-2012

Revised Date : 13-Jun-2013

Accepted Date : 18-Jul-2013

Article type : Original Article

Mapping sub-pixel fluvial grain sizes with hyperspatial imagery

Martin Black (1, 2), Patrice Carbonneau (1), Michael Church (3), Jeff Warburton (1)

(1) Department of Geography, Durham University, Lower Mountjoy South Road, Durham, DH1 3LE, United Kingdom

(2) British Antarctic Survey, High Cross Madingley Road, Cambridge, Cambridgeshire CB3 0ET, United Kingdom (email: marack97@bas.ac.uk)

(3) Department of Geography, Faculty of Arts, The University of British Columbia, 1984 West Mall, Vancouver, BC V6T 1Z2, Canada

Short Title - Mapping sub-pixel grain sizes

ABSTRACT

This paper presents an investigation of image texture approaches for mapping sub-pixel fluvial grain-size features from airborne imagery, allowing for the rapid acquisition of surface sand and coarse fraction (>1.41 mm) grain-size information. Imagery at 30 mm resolution

This is an Accepted Article that has been peer-reviewed and approved for publication in the *Sedimentology*, but has yet to undergo copy-editing and proof correction. Please cite this article as an "Accepted Article"; doi: 10.1111/sed.12072

was acquired over four gravel bars from the Fraser River (British Columbia, Canada). Combined first-order and second-order image texture approaches (windowed standard deviation filter and the grey level co-occurrence matrix) were used. First-order image texture, through the application of a standard deviation filter and subsequent thresholding was used to detect the presence of surface sand, with optimal accuracy achieved at 91 ± 1.9%. A wide-ranging parameter space investigation was used to derive optimum parameters for the grey level co-occurrence matrix. Subsequently first- and second-order image textures were used in multiple linear regression to achieve good calibrations with several sub-pixel grain-size percentiles; relative error at 1.44%, 3.18%, 6.80% and 10.6% for D5, D16, D35 and D50, respectively. The larger percentiles of D84 and D95 had relative errors of 24.7% and 29.7%, respectively. The breakdown of calibration precision for larger percentiles is attributed to a 'pixel averaging effect'. It is concluded that multispectral imagery is not required, because sufficient image texture information can be derived from standard colour imagery. Recommendations are suggested for application of this method to other localities and datasets, thus reducing exhaustive parameter searches in future studies.

Key words: Fluvial grain size, airborne remote sensing, digital image processing, sub-pixel features, hyperspatial imagery, image texture, grey level co-occurrence matrix.

INTRODUCTION

Research into fluvial systems is often based on field studies that are inevitably limited in terms of spatial coverage and resolution (Fausch *et al.*, 2002). However, technological advances are changing the way river scientists map, manage and analyse rivers (Marcus & Fonstad, 2008). Among these new technologies, the increasing acquisition and processing of hyperspatial imagery (<100 mm spatial resolution; Rango *et al.*, 2009; Carbonneau and Piegay 2012) is revealing great potential for catchment scale mapping at unprecedented resolutions (Carbonneau *et al.*, 2012).

Grain-size information for gravel bed rivers is important in a wide variety of contexts, providing information to guide the development of flood defences and maintaining navigability, biodiversity and ecological integrity within large rivers (Klingeman, 1998). Within the remote sensing literature, two main categories of techniques are discussed for

extracting grain-size information from digital imagery, close range 'photosieving' techniques and reach scale assessments using image texture analysis. Photosieving techniques are based on images of sediment collected at ground level where each grain is imaged by several pixels; images are rapidly acquired in the field and grains manually measured from the image at a later date (Ibbeken & Schleyer, 1986). Thus, photosieving reduces the need for surface gravel sampling and increases the amount of collected data. More recently, automated procedures to extract grain-size information from digital images have been developed. These procedures use image segmentation and boundary detection approaches to emulate the way a human user would delineate grains (McEwan *et al*., 2000; Butler *et al*., 2001; Graham *et al.* 2005a,b; Chung & Chang, 2012). Alternatively, statistical methods such as mathematical morphological operators (Pina *et al*., 2011), spatial autocorrelation (Rubin, 2004) or spectral autocorrelation (Buscombe, 2008; Buscombe *et al.*, 2010; Buscombe and Rubin 2012a,b) can be used. Given the requirement for pixel sizes much smaller than grain sizes, photosieving uses terrestrial imagery.

In the case of airborne, reach scale studies, image texture applied to hyperspatial imagery has been used to extract grain-size information (Carbonneau *et al*., 2004; Verdu *et al.*, 2005). Image texture analysis involves quantifying the differences in pixel intensity values within a region of neighbouring pixels. These operations can be split into two types; first-order methods which are simple statistical measures where pixel neighbour relations are not considered and second-order methods which consider the spatial relation and spatial structure of the pixels. Some common measures of first-order image texture include mean, variance, and range of pixel intensity values within a local neighbourhood. For second-order methods the grey level co-occurrence matrix (GLCM) (Haralick *et al*., 1973; Haralick, 1979) is perhaps the best-known texture measure.

Early applications of airborne grain-size mapping were limited to gravels, cobbles and boulders. Sand particles, being much smaller than the pixel size, remained undetectable (Carbonneau, 2005). However, preliminary results presented by Chandler *et al.* (2004) suggest that simple first-order texture measures are sufficient for detecting the presence of surface sand, whilst the work of Carbonneau *et al.* (2004) and Verdu *et al.* (2005) showed that second-order texture approaches can be used to extract multiple grain-size percentiles. However, measures such as the GLCM require several input parameters (for example, directional offset, grey levels and window size); an extensive parameter investigation also increases data processing time. Carbonneau *et al.* (2004) and Verdu *et al.* (2005) investigated

only a small sub-set of GLCM parameters and did not address the applicability of these methods for detecting sub-pixel grains.

In this paper, a detailed investigation into first-order and second-order image texture approaches is presented, expanding the parameter space investigated by Carbonneau *et al.* (2004) and Verdu *et al.* (2005), with the main aim of extracting sub-pixel fluvial grain-size features from hyperspatial imagery. The preliminary investigations of Chandler *et al.,* (2004) were limited; hence, first-order image texture methods are re-examined in more detail. Second-order image texture methods (through the GLCM and its expansive parameter space) were applied to the coarser (>1.41 mm) fluvial sediment size fraction. These tasks were formulated into two research objectives:

- To investigate first-order image texture methods for producing maps of surface sand areas.
- To investigate first-order and second-order image texture methods (through the GLCM) for deriving grain-size distributions for the coarse (>1.41 mm) size fraction.

METHODS

Study Area

The Fraser River (British Columbia, Canada) is one of the large rivers in North America, draining an area of approximately 233,000 km^2. The river rises in the high plateaux and mountains in the central part of the province and descends a series of canyons to enter the distal Fraser Valley where it receives its final major tributary, Harrison River. Mean annual flow at Mission, downstream of Harrison River is 3410 m^3s^{-1} and mean annual flood is 9710 m^3s^{-1}. Gravel is the predominant bed sediment type in the 100 km 'gravel reach' of the lower Fraser, between Hope and Mission (Figure 1); however there are also significant quantities of sand. The sediments show both downstream and vertical patterns of sorting within the channel system (Rice & Church, 2010), becoming finer and more sand-rich downstream. Four gravel bars within the 'gravel reach' were selected for data acquisition: Queens Bar, N Bar, Calamity Bar and Harrison Bar (Figure 1). These bars are located between 110 km and 120 km upstream of Sand Heads (mouth of the Fraser River).

Airborne Hyperspatial Image Acquisition

In March 2012, hyperspatial imagery was acquired over Queens Bar, N Bar, Calamity Bar and Harrison Bar by the DTM Mapping Corporation (http://www.dtm-global.com). Eight-bit imagery was collected using a Vexel Imaging UltraCamX (Vexcel Imaging GmbH, Graz, Austria) at a spatial resolution of 30 mm. Imagery was acquired in Near Infrared, Red, Green and Blue bands. Following the collection of raw imagery image enhancement was performed during the orthorectification stage, through the application of an image dodger. The image dodger performed histogram matching on the overlapping region of the neighbouring images to normalise the intensity values between individual images. Due to the consistent (cloudy bright) lighting conditions during acquisition the effects of the image dodger on pixel intensities were minimal. Images were automatically mosaicked and rectified, producing *ca* 230 image tiles covering the areas shown in Figure 1.

Ground truth grain-size data

In the field, 23 vegetation-free gravel sites were randomly selected for surface grain-size analysis, on Queens Bar (11), N-Bar (5), Harrison Bar (3) and Calamity Bar (4). Sample sites were visually homogeneous over several metres. At each of these sites a rectangular frame was placed over a 1.0 x 0.8 m area (Figure 2). Within the frame area, the surface grains were spray-painted and subsequently, painted grains were collected and measured; a technique commonly known as paint-and-pick (Lane, 1953; Church *et al*., 1987). For sediment larger than 8 mm, field templates were used to measure the grains, with the remaining smaller grain fraction being stored for later laboratory sieving. In the laboratory, samples were sieved to 1.41 mm; weights were calibrated to particle counts and converted to a full distribution. Geolocation of the field sites was carried out using a Trimble 5700 differential Global Positioning System (GPS; Trimble Navigation Limited, Sunnyvale, CA, USA). Post-processing of the GPS data was carried out using the Canadian Spatial Referencing System (CSRS) online GPS Processing service (http://www.geod.nrcan.gc.ca/products-produits/ppp_e.php). With an integrated base station time of around seven hours, the GPS points have an estimated precision in X, Y and Z of ±20 mm.

Image texture and grain-size features

Sand

To assess the relation between image texture and the presence of surface sand, a collage of three image tiles (15 x 15 m) was created (Figure 3). The collage image encompasses a variety of features that may influence image texture calculations within the study region including areas of gravel–sand and wet–dry sand transitions, natural features such as log jams, and areas of human disturbance (tyre tracks). All of these features introduce variations in the intensity levels of the image and, therefore, image texture will be sensitive to these intensity changes. To facilitate accurate assessment, non-sand areas were manually delineated on the composite image using a Graphical User Interface (GUI) (Figure 3). To give an idea of the likely error associated with manual delineation, five independent users delineated a sand/gravel patch in the same image and their results diverged by 1.9% (*ca* 0.8m^2 in real terms).

A standard deviation moving window was applied across this composite image over a range of window sizes (Chandler *et al.,* 2004). The resultant texture image was thresholded at increasing values to produce binary images of sand, non-sand. The relation between image texture values and sand was assessed to confirm the hypothesis that low texture values are linked to the presence of surface sand. Assessment was made using a figure of merit (Klug *et al*. 1992; Pontius *et al*. 2008) to give a percentage accuracy of classification of 'sand' pixels, as shown in Eq. 1:

$$FoM = \frac{px_{ov}}{px_{un}} \quad (1)$$

where px_{ov} is the number of mutually classified pixels in the manually delineated image and the texture thresholded image (i.e. correctly identified pixels), and px_{un} is the number of unique pixels in either image (i.e. pixels representing both errors of commission and omission). The figure of merit index is used for the analysis of spatial patterns (Klug *et al*. 1992; Perica & Foufoula-Georgiou, 1996), as it is a dimensionless index with a theoretical range from 0 to 1, where 0 is no overlap and 1 is perfect overlap.

Coarse Fraction

The relation between image texture and seven, field sampled, coarse fraction grain-size percentiles (D_5, D_{16}, D_{35}, D_{50}, D_{65}, D_{84} and D_{95} determined from the field samples) was investigated using both first-order and second-order image texture and linear regression between image texture values and grain-size values for each percentile. First-order image texture was assessed through the application of a standard deviation filter and second-order image texture was investigated through the GLCM within a large parameter space. Both first-order and second-order image texture methods were then applied through Multiple Linear Regression to assess their combined relation with each of the seven coarse fraction grain-size percentiles.

First-order Image texture – Standard Deviation Filter: In a manner similar to the assessment of image texture and sand, a standard deviation filter ranging from 3 x 3 in steps of two pixels to a maximum of 69 x 69 pixels was applied and subsequently linearly regressed to the seven coarse fraction percentiles. Each combination of window size and image band was computed, leading to a total of more than 3,100 first-order image texture calculations.

Second-order Image texture – Grey Level Co-occurrence Matrix : Second-order texture measures using the GLCM were assessed through a similar process of image texture calculation and subsequent linear regression with the seven percentiles. When calculating a GLCM, there are several parameters to consider; window size $f(x,y)$, directional offset $O(x,y)$, number of grey levels L, the wavelength band of the image used (NIR, R, G, B) and the statistic calculated. A GLCM can be defined as follows: let $O(x,y)$ be an operator that defines the spatial relation of the two pixels relative to each other, on a sub-image $f(x,y)$ (i.e. a window extracted from the larger input image, I) with L possible intensity levels. Intensity levels L (grey DN levels) are the range of pixel values represented in the GLCM; for example an 8-bit image can be processed at $L = 256$ to produce an 8-bit GLCM with a size of 256 x 256. However, it is common practice to 'downsample' grey levels before calculating a GLCM as high numbers of grey levels are computationally expensive. The GLCM, $\boldsymbol{G}$, is a matrix whose element $\boldsymbol{G}(i,j)$ is the number times that the pixel pairs with intensity levels z_i and z_j occur in the image f at the positions specified by $O(x,y)$.

Consider the example shown in Figure 4 (Gonzalez and Woods, 2008) for image f where $L = 8$, and O is defined as 'one pixel to the right'. This example shows that element (6,2) of $\boldsymbol{G}$ has a value of 3, as there are 3 occurrences in image f of a pixel value of 6 where its neighbour to

the immediate right has a value of 2. In this example, the window size is equal to the size of the sub-image *f* (for example, 6 x 6). Following the calculation of this GLCM, statistical descriptors can be calculated reducing the GLCM to a scalar value. This value is placed in the texture image, *T*, at the location of sub-image *f*. Therefore the resolution of the texture image, *T*, is proportional to the window size (size of sub-image) used to process input image, *I*. For example, a 1024 x 1024 input image, *I*, processed with a window size, *f(x,y)* of 64 x 64 produces a texture image, *T*, with size of 16 x 16 (with no overlap of adjacent windows).

In order to reduce the number of GLCM calculations to manageable processing times, a limited parameter space was investigated. Following the recommendations of Clausi (2002), the 'preferred statistic set' was investigated; GLCM contrast, correlation and entropy (Eqs 2a, 2b and 2c):

$$
\begin{aligned}
(a) GLCM_{con} &= \sum_i \sum_j (i-j)^2 p_{ij} \\
(b) GLCM_{cor} &= \frac{\sum_i \sum_j (i,j)\, p(i,j) - \mu i \mu_j}{\sigma_x \sigma_y} \\
(c) GLCM_{ent} &= \sum_i \sum_j p_{ij} \log\left(p_{ij}\right)
\end{aligned}
\qquad (2)
$$

where *(i,j)* represents the image coordinates, *p(i,j)* represents the normalised GLCM matrix value at the point *(i,j)*, $\sigma(i)$ $\sigma(j)$ represents standard deviation of the GLCM row *(i)* or column *(j)* and $\mu(i)$ $\mu(j)$ represent the mean of the GLCM row *(i)* or column *(j)*. This 'preferred statistic set' combines the GLCM statistics which are independent and not correlated (Clausi, 2002). Table 1 shows the parameters investigated. Offsets are given as *O(x,y)* and calculated only in cases where the Offset is smaller than the window size. A symmetrical GLCM was calculated (Haralick *et al.,* 1973); for example, the sum of two GLCMs with offsets *O(0,+1)* and *O(0,-1)* is equal to the symmetrical GLCM of *O(0,+1)*.

The full parameter space outlined above led to more than 84,000 sets of GLCM parameters, each calculated on 23 images resulting in a final total of over 1.9 million image texture calculations.

Combined First-order and Second-order Image texture using Multiple Linear Regression: Verdu *et al.,* (2005) observed increased accuracy of calibrations with multiple linear regression (MLR) of several image texture measures. The increased accuracy is probably a result of the increased information provided by several texture measures and the combination of this information through MLR, straightforwardly possible with independent image texture measures. To further test this finding, the 'best performing' parameter sets (high r^2 and low MSE) from first-order image texture (standard deviation) and second-order image texture (contrast, correlation and entropy) were selected for MLR.

Leave-one-out cross-validation (Friedman *et al*., 2001) was used to give a precise estimate of MSE (cross-validated Mean Square Error: MSE_{cv}). Leave-one-out cross-validation involves using a single observation from the original sample as validation data, and the remaining observations as training data. The process is iterated until each observation in the sample is used once for validation.

Grain-Size Mapping: Workflow

Following the investigations of first- and second-order image texture measures for deriving surface grain size information outlined in the *Sand* and *Coarse fraction* section above, a workflow was developed for batch-processing of all of the hyperspatial image tiles from the study region. The optimal results from those investigations were used to guide this workflow. All of the image tiles from the study area were processed to produce continuous grain-size maps for the entire study region. The workflow is summarised in Figure 5.

First, the raw image tile was segmented using the Otsu method (Otsu, 1979) to remove water and vegetation. This method sets a threshold by minimising the interclass variance of the pixels either side of the threshold value. A visual assessment of the imagery ensured that the threshold value was appropriate for the imagery. The threshold value may then be manually adjusted as required to ensure that vegetation and water areas are appropriately masked. Masking of these areas is not explicitly required to calculate surface sand and grain-size maps, because vegetated and water surfaces can be masked at any stage. However, masking earlier in the workflow avoids unnecessary computation in the latter stages.

A standard deviation filter was then applied and thresholded to produce surface sand content. Remaining pixels (i.e. those not classified as water and vegetation or sand), were then processed through the GLCM and MLR to produce a surface grain-size distribution.

RESULTS

Ground truth grain-size data

Figure 6 shows the full grain-size distribution for all 23 coarse fraction sites, truncated at 1.41 mm. Table 2 shows summary statistics, with percentile data being linearly interpolated between sieve data points shown in Figure 6. The samples represent a good range for investigation of texture detection methods.

First-order image texture calibration: Sand

Figure 7 shows the percentage accuracy for each window size calculated using the FoM with an initial threshold value of 3.5. Highest accuracies are found at the smaller window size, with a window size of 3 x 3 pixels producing the best result. Interestingly, the choice of band has little effect, with all four bands converging at the highest accuracies.

The influence of changing threshold values was investigated (Figure 8). Lower threshold values result in lower accuracies, until a peak in accuracy is reached around 3.5. A broad peak in accuracy is observed for threshold values above 3, with a slight decline in accuracy beginning at threshold values greater than 4.5.

First-order and second-order image texture calibration: Coarse fraction

First-order image texture

Figure 9 shows results of calibrations with the D_{50} grain-size percentile. Very similar coefficient of determination (r^2) values are seen from D_5 to D_{65}. For the largest percentiles, D_{84} and D_{95}, the relation begins to break down and much poorer results are observed, particularly for D_{95} (Figure 10). Similar to the relation between first-order texture and sand (see *First-order image texture calibration: Sand* section), the band selected does not greatly affect the results; very similar calibrations are seen using either the red or NIR bands, with only the blue band producing noticeably lower r^2 values.

Table 3 shows the parameters of the best performing standard deviation filter for each percentile, later used in multiple linear regression (see *Multiple linear regression using first-order and second-order image texture* section below).

Second-order image texture

For each GLCM statistic (contrast, correlation and entropy), there were *ca* 28,000 parameter sets; containing all combinations of window size, offset (x), offset (y) and grey levels for each of the four image bands (R, G, B and NIR) for each of the seven grain-size percentiles (D_5 through to D_{95}). Visualisation and interpretation of these results can be difficult. To provide an initial insight into the parameters, for each percentile the top 1000 runs (sorted by r^2 values) were extracted and split into two spectral groups; RGB and NIR. This grouping allows for an assessment of the use of standard RGB imagery versus multispectral (RGB and NIR) imagery. Figure 11 shows a bar chart of r^2 results for the two groupings for each percentile. Reasonable results ($r^2 > 0.6$) are achieved for all percentiles up to D_{65}, after which results begin to deteriorate for the larger percentiles D_{84} and D_{95}.

In all cases, RGB and NIR produced very similar r^2 values for the best performing runs; RGB outperformed NIR, with the exceptions of D_5 and D_{95} where NIR r^2 values were slightly larger (<0.1) than their RGB equivalent.

Similarly, 16 grey levels were dominant within the 'top 1000' runs; Figure 12 shows the frequency of 16 grey levels within the 'top 1000' parameter sets; it is dominant (frequency >70%) in percentiles up to and including D_{84} for both RGB and NIR. Only when D_{95} is reached does its dominance decline; at D_{95} calibrations also greatly decline (see Figure 11). Hence, there is little difference between RGB and NIR bands, with RGB slightly outperforming NIR in all cases.

Some parameters can be ruled out as their influence is negligible. For example, regardless of the choice of band similar relations between image texture and grain size are seen (Figure 11). Similarly, 16 grey levels showed clear dominance; hence this parameter can also be fixed (Figure 12). The remaining parameters, window size and offsets (x,y) did not show such clear patterns; each combination varied with different percentiles, however peaks in r^2 occurred with window sizes largely above 20 x 20 pixels. No clear pattern could be discerned for the

offset (x) and offset (y) parameters as they were the most varied across all percentiles, although slight north–east, south–west trends were noted (offset (x) and (y) values >1 representing north–east, south–west), probably linked to imbrication of sediment in the field.

To investigate the influence of window size and offsets (x,y) on image texture–grain size relations a three-dimensional parameter space was established. Figure 13 shows three two-dimensional extracts from this parameter space to visualise the parameters of offsets (x and y) and window size for D_{50}. Offsets have an area of high r^2 located around offset (x) of 0, and offset (y) of 0, with a similar area of high performance with offset (x) values around 6; optimal offsets are (0,5) for x and y respectively (Figure 13A). A very clear boundary is evident when considering variations in window size (Figure 13B and C), with notably high r^2 values prevalent above window sizes of *ca* 35. Variations in offset (x) values (Figure 13B) seem to show much less sensitivity, with high r^2 values seemingly dependant only on window size; once in the optimal window size region (>35). For the offset (y) (Figure 13C), peak performance is clustered around values of 5, although similar performance is noted across all offsets above 4, with decreasing r^2 values for the lowest offsets.

Patterns similar to those shown in Figure 13 were noted for most of the other grain percentiles except for the largest percentiles, D_{84} and D_{95}, for which the relations begin to break down and large, clear peaks in performance (such as those seen in Figure 13) are much less clearly defined.

Following this investigation, the best performing parameter set for the three independent GLCM statistics (contrast, correlation and entropy) was established for each percentile. These parameter sets are shown in Table 4.

Multiple linear regression using first-order and second-order image texture

Multiple linear regression (MLR) was used to relate data from first-order and second-order image texture to grain size. The best performing parameter sets were selected for each GLCM method (contrast, correlation and entropy) and combined with the best performing standard deviation measure (Tables 3 and 4). Multiple linear regression was applied to these parameters, and leave-one-out cross-validation used to assess the results (Friedman *et al.*, 2001). Table 5 shows the MLR coefficients, and resulting statistics for each percentile. The highest r^2 and lowest MSE values are found in the lower percentiles, with the best calibration

found for D_5. Reasonable calibrations are seen up to D_{65}, with MSE at 17.2%. Calibrations are poorest for D_{95} with MSE at 29.7%. For each percentile, the grain size was calculated, and compared to observed grain size (Figure 14).

Grain-size maps: Sand and Coarse fraction

Figure 15 shows a sample D_{50} map produced following the workflow outlined in the *Grain-size mapping: workflow* section. These images are gridded at variable spatial resolutions. Sand classification maps are resolved at 81 cm^2 (window size of 3 x 3 pixels), whilst coarse fraction percentiles have varying resolution. The spatial resolution is a product of the largest window size used; the coarsest resolution was that of D_5, at *ca* 4.3 m^2 (largest window of 69 x 69 pixels).

DISCUSSION

Results show that first-order and second-order image texture approaches are suitable for the detection of surface sand and the extraction of surface grain-size percentiles from hyperspatial imagery. Unlike previous approaches using image texture, the applicability of these techniques for extracting both surface sand content and a grain-size distribution has been shown. The preliminary findings of Chandler et al. (2004) are confirmed; a simple first-order texture measure proved adequate for detection of surface sand features. Similarly, following a wide-ranging parameter space investigation and multiple linear regression using first-order and second-order image texture, a technique suitable for extracting the finer scale grain-size percentiles (D_5 through to D_{65}) was also achieved. Both of these techniques improve on current methods by explicitly extracting sub-pixel grain-size distributions; however, an important constraint is noted as the pixel resolution is approached *(*see *First-order and second-order image texture grain-size calibration: Coarse fraction* section below*).*

First-order image texture grain size calibration: Sand

Investigation of image texture and sand revealed that simple thresholding following the application of a windowed standard deviation filter can produce maps of surface sand with peak accuracies of *ca* 91%. Interestingly, optimal accuracies are achieved regardless of the choice of image band used (Figure 7). However, the threshold value selected affects the accuracy of the resulting sand classification. In this particular study region, optimal accuracy

was achieved with a threshold value of 3.5, but high performance (*ca* 90%) was noted for threshold values between 2.5 and 4.5 (Figure 8). The collage image used to assess this technique (Figure 3) contained transitions between wet and dry sand, transitions between surface sand and gravel, logs and tyre tracks. These features represent areas where pixel values vary in intensity and thus have a distinct textural signature. Conversely, in homogenous areas (larger than the window size) where sand is present pixel intensity values show little variation and thus can be easily detected. Figure 16 shows the differences in classifications with changing threshold values, calculated on the green band of the composite image.

Selecting low threshold values can erroneously remove sand areas from the classification. This effect can be seen in Figure 16B and C, where particular features such as transitions between wet and dry sand, and tyre tracks have been misclassified. Increasing threshold values removes these features; however, even with threshold values in the optimal accuracy region (Figure 16D and E) errors are still present. Perhaps the most obvious of these is the transition area between the three images which make up the collage image itself. Even though these areas are mostly sand, they still have abrupt changes in intensity values and, hence, have high texture values which result in misclassification. Whilst this effect would be negated using full image tiles, it serves as a clear example to highlight how sensitive this method is even to slight changes in pixel intensity values. Areas where abrupt changes in pixel intensity values occur may be misclassified. This could occur within areas entirely composed of sand; features such as shadows on the stoss or lee side of dunes and ripples, transitions from wet to dry sand, and human features such as tyre tracks are just a few examples which could cause pixel intensity differences. Therefore, it is recommended that threshold values be adjusted depending on the imagery and the user's purpose. For example, in order to minimise errors of omission and assuredly classify all areas of surface sand the user may select a slightly higher threshold value with the knowledge that there may be some errors of commission (such as homogenous areas of fine gravel which may produce a low textural signature, and hence may be classified as sand).

These results support the findings and suggestions of Chandler *et al.,* (2004) that there is enough information present in standard colour imagery to yield accurate maps of surface sand content. Accuracies achieved here represent an improvement on those presented by Chandler

et al., (2004) in terms of sand classification, probably due to the simple texture thresholding approach and the improved image quality (the aerial imagery used here was acquired in dry conditions with consistent lighting). This texture approach is beneficial as computational cost is modest, meaning large images can be easily and quickly processed, enabling rapid mapping of entire reaches. The sand calibrations derived here can also be applied to grey-scale imagery because only one band is required for the computation of image texture; this allows for potential exploitation of archives of grey-scale imagery. However, it must also be noted that the hyperspatial resolution is a key factor in allowing the sand mapping method to function. Only homogenous sand areas greater than three times the pixel size can be mapped using this method (i.e. sites which occupy *at least* the area covered in a 3 x 3 pixel window). Furthermore, the excellent radiometric quality delivered by the Vexel UltraCamX (Vexcel Imaging GmbH) was undoubtedly another key factor in the success of the method.

First-order and second-order image texture grain-size calibration: Coarse fraction

A combined MLR approach encompassing all texture measures provides the best calibrations, a finding similar to that of Verdu *et al.,* (2005). All of the derived grain-size percentiles in this study are smaller than the image resolution of 30 mm. Interestingly, relations become much weaker as the pixel resolution is approached, with the strongest relations found for the finer percentiles (D_5 through to D_{65}).

Theoretical considerations; the 'pixel averaging effect'

Image texture and grain-size relations begin to deteriorate above D_{65}. The breakdown of calibrations for the coarser percentiles is attributed to those percentiles lying within the transition from 'pixel averaged texture' to 'actual grain texture'.

'Pixel averaged texture' is a direct result of the finer grain-size percentiles being much smaller than the pixel resolution (30 mm); hence these grain sizes are sub-pixel. Therefore, one pixel is an averaged measure of a population of several grains. Within homogeneous grain-size patches this leads to low intensity variance between neighbouring pixels and 'smooth' image texture patterns; these 'smooth' textures calibrate well with the grain size of the smaller percentiles.

As grain size approaches the pixel resolution a transition is gradually made from 'pixel averaged texture' to 'actual grain texture'. 'Pixel averaging' reduces as smaller populations of individual grains are represented in one pixel, hence the variance in image texture values between neighbouring pixels increases and relations between image texture and grain size become unstable. In this study, the coarser grain size percentiles of D_{84} and D_{95} are an example of this; they lie in the transition area between 'pixel averaged texture' and 'actual grain texture', and poorer relations between grain size and image texture are noted as a result.

After the threshold is fully crossed, image texture values are then directly related to 'actual grain texture' as one pixel is no longer an average measure of a population of several grains. Image texture and grain-size relations begin to stabilise again (Figure 17). Verdu *et al.,* (2005) found strong calibrations for intermediate and larger percentiles (D_{50} and D_{84}) using 3 mm resolution imagery and measuring 'actual grain texture'.

When considering grain sizes that lie below the pixel resolution, there is a clear link between the spatial resolution of the imagery and the window size used to calculate image texture. For example, higher resolution imagery requires larger window sizes, and coarser spatial resolution imagery requires smaller window sizes. This is to offset the averaging that takes during image acquisition; with coarser resolution imagery there is greater averaging due to the larger spatial coverage of one pixel (and the subsequent averaging of a larger population of grains). This is corroborated by comparison with other studies. Carbonneau *et al.,* (2004) observed peak performance at window sizes around 33 x 33 pixels using 30 mm resolution imagery. However, a later study using coarser 10 cm resolution imagery noted peak performance with a smaller 20 x 20 pixel window (Carbonneau, 2005).

Parameter space investigation; which parameters are important?

First-order image texture measures present the simple situation in which the user has only to consider which combination of band and window size to adopt. Figure 9 shows an investigation of these parameters. Interestingly, there is a high degree of similarity in the results irrespective of the band used; namely, red, green, blue and NIR bands produce very similar results. This is probably due to the high degree of correlation amongst the RGB–NIR bands in the imagery and the spectral similarity of sediment in these bands; hence image texture calculations produce very similar results irrespective of the band used. Similarly,

second-order image texture also showed that there is little additional benefit gained from having an NIR band.

For the second-order GLCM parameter of grey levels, a clear pattern could be discerned. Within the percentiles that produced robust relations (D_5 to D_{65}), over 70% of the 'top 1000' parameter sets had 16 grey levels (Figure 12). Similarly, Table 4 shows this pattern with a distinct dominance of 16 grey levels. The resampling of grey levels to this smaller value may have introduced some stability into the texture calculations and reduced grey level noise; conversely the expansion of grey levels, up to 64 (and beyond, such as 128 or 256) increases the amount of information captured in the GLCM, because there is less resampling. However, the downside is that there is much greater variance in the GLCM itself, as well as within the GLCM statistics. Subsequent image texture and calibrations begin to break down as a result. This suggests that the downsampling of grey levels is an acceptable practice (in line with findings of Carbonneau, 2005), and is even beneficial.

Patterns could also be discerned for window sizes and offsets for the reliably estimated percentiles (D_5 to D_{65}). An illustrative example of this is shown in Figure 13. Distinct areas of higher performance were evident, most clearly articulated for window sizes. A clear threshold was observed; performance greatly deteriorated with window sizes smaller than *ca* 35 x 35 pixels. The optimal window size is reached when enough pixels are present to produce stable calibrations; in this instance, this occurs with window sizes above 35 x 35 pixels (cf. 'pixel averaging effect'; *Theoretical considerations; the 'pixel averaging effect'* section).
Offset directions (x and y) had their own high performance areas respectively; however patterns are more difficult to interpret. Predominantly north–south, and slight north-east/south-west GLCM orientations (using a symmetrical GLCM) (Table 4) were noted (in GLCM coordinate space, where north–south represents offsets in the *y* direction, and east–west the *x* direction). A potential reason for the trend in GLCM orientation could be the imbrication of sediment in the field; GLCM orientations are the same as the downstream flow direction of the river.

Each of the independent GLCM statistics (contrast, correlation and entropy) was calculated with the premise that they would be later used in MLR; but reasonable results ($r^2 > 0.65$) were achieved for percentiles up to and including D_{65} without the use of MLR. Performance was similar irrespective of the method used, however both correlation and entropy rapidly deteriorated for the larger percentiles (D_{84} and D_{95}), suggesting that contrast may produce the

most stable relations when considering the full seven point coarse fraction grain-size distribution. In assessing the applicability of these techniques at other study localities and with differing scales of imagery, a reduced parameter space is recommended. Multispectral imagery is not required, because similar relations are found using only standard colour imagery. Future studies need consider only the parameters of window size (where the minimum window size is set according to the image resolution), and offsets. Offsets should be investigated with prior knowledge of sediment imbrication in the field, as it is likely that the optimal GLCM orientation will be coincident with any imbrication. Remaining parameters can be set as desired; if MLR is used, the independent statistic set (contrast, correlation and entropy) is advised, and contrast is recommended if no MLR is used. Grey levels can be fixed at 16 (or perhaps even reduced).

Grain-Size Mapping Considerations

Figure 15 shows a D_{50} grain-size map calculated for N bar, at a spatial resolution of 2.34 m^2 (window size of 51 x 51 pixels). Coarser resolution is noted compared to Carbonneau *et al.,* (2004) and Verdu *et al.,* (2005) as a result of block processing at larger window sizes. This D_{50} map was produced following the workflow outlined in the *Grain-size mapping: workflow* section. The final outputs from this processing chain are eight images; a surface sand classification, and an image for each of the seven grain-size percentiles.

Consideration must be given to the MSE values achieved for each percentile, and errors must be accounted for when using calculated grain sizes for other applications such as modelling. Significant uncertainty exists for the larger percentiles, particularly D_{84} and D_{95}; however the finer grain fractions provide fairly precise estimates compared to field sieved data, and are much improved compared to previous remote sensing methods.

The direct applicability of the actual parameters and MLR coefficients presented here for deriving similar results at other field sites is difficult to assess due to the lack of a similar dataset in a different location. It is expected that grain morphology, a consequence of grain lithology, may introduce variability in the parameters of the calibration equations. However, the same methodology and workflow (*Grain-size mapping: workflow* section) are directly transferable to other sites, although local calibration may be required. Parameter investigations need not be as exhaustive as those presented here, and can follow the general recommendations outlined at the end of the *Parameter space investigation; which parameters are important?* section.

Consideration must be given to computational power required to process expansive parameter spaces. Of all the parameters, the dominant control on CPU time is window size; smaller windows require the processing of more blocks, therefore more time is spent calculating GLCMs. The CPU time (seconds) is inversely proportional to window size w, with an approximate relation of $45(w^{-2})$ where w is the window size. This should then be multiplied by the total number of blocks to gain the approximate CPU time to process an entire image.

Limitations

Several limitations and areas of uncertainty exist in this study. An increased number of ground sampling sites would provide a better indication of calibrations and other methods of measuring grain size (for example, Wolman sampling) could have been employed to aid in validation of results, particularly for the sand sites. An increased number of sites would also allow for the retention of some data for grain-size validation, rather than using cross-validation. Using the paint and pick technique, paint may have penetrated the interstitial space between surface and buried grains; hence some sub-surface grains may have been incorrectly collected and sampled, introducing some uncertainty into the results. Paint may have adhered smaller, particularly sand and silt, grains to larger particles, thereby introducing a bias into the finer grained fraction of the distribution (or in some cases it may have acted to remove finer grained material from the sample). Conversion of the finer grained material from weights to grain counts may have also introduced slight error within the data.

The field sampling might introduce an additional difficulty for unbiased representation of the largest sizes. Large clasts are least common in a single sample, so a large number of samples must be recovered in order to assure that percentiles at the upper limit of the size distribution are correctly assigned (Church *et al*., 1987). However, in the present case, the largest grains (of order 22 mm) each occupy about 0.04% of the field sample area and the problem should not be significant.

A particular area of uncertainty exists in reference to the aerial imagery itself. The georeferenced image tiles supplied by DTM Mapping Corporation had undergone some element of pre-processing, the summary effect of which has not been investigated. Raw, unprocessed image tiles were also supplied; however the influence of significant georeferencing issues and lack of perspective correction meant that the raw imagery introduced a much greater source of positional error; and thus could not be calibrated due to uncertainty in georeferencing.

CONCLUSIONS

This study has investigated the relation between image texture and surface grain size using hyperspatial imagery. Detailed investigation of first-order and second-order image texture approaches for extracting sub-pixel grain-size information have shown convincingly that simple first-order measures are suitable for delineating surface sand features, whilst a combined approach of first-order and second-order image texture can extract sub-pixel grain-size percentiles for the coarse fraction. This study represents a significant step forward in terms of the applicability of image texture approaches for deriving sub-pixel grain-size features from hyperspatial imagery. The main conclusions are as follows:

- The sand fraction can be automatically delineated with a peak classification accuracy of *ca* 90% using simple image texture thresholding.

- Coarse fraction (>1.41 mm) grain-size percentiles can be extracted using combined first-order and second-order image texture and multiple linear regression; relative error in this study was 1.5%, 3.2%, 6.8% and 11% for D_5, D_{16}, D_{35} and D_{50}, respectively. The largest percentiles of D_{84} and D_{95} had relative errors of 25% and 30%, respectively.

- Multispectral imagery (i.e. the additional of a near-infrared band) is *not* required, as standard colour imagery is sufficient.

The final workflow presented in the *Grain-size mapping: workflow* section allowed for the production of surface sand classification and a seven point coarse fraction grain-size distribution covering the major sand and gravel bars of Queens Bar, N Bar, Calamity Bar and Harrison Bar located within the gravel reach of Fraser River. The limited number of field sites for calibration and validation (14 for sand and 23 for the coarse fraction) is noted as a point for expansion in future studies. This method allows for a rapid acquisition of a seven point grain-size distribution and map of surface sand content for large, vegetation-free sediment areas at a much higher spatial resolution than can be obtained through standard field techniques.

ACKNOWLEDGMENTS

MB was supported by a Durham University Research Bursary. Acquisition of the hyperspatial imagery and field operations on Fraser River were supported by a Discovery

Grant from the Natural Sciences and Engineering Research Council of Canada and a contract from the Canadian Department of Fisheries and Oceans (awarded to MC). The cooperation of members of DTM Mapping Corporation is gratefully acknowledged. Dave Reid and Matt Chernos are gratefully thanked for their support in the field. Reviewers are thanked for their detailed comments on earlier versions of this manuscript.

References

Buscombe, D. (2008). Estimation of grain-size distributions and associated parameters from digital images of sediment, *Sedimentary Geology* **210**(1-2): 1 – 10.

Buscombe, D. and Rubin, D. (2012a). Advances in the simulation and automated measurement of well-sorted granular material. part 1: Simulation., *Journal of Geophysical Research* **117**: F02001 doi: 10.1029/2011JF001974.

Buscombe, D. and Rubin, D. (2012b). Advances in the simulation and automated measurement of well-sorted granular material. part 2: Direct measures of particle properties., *Journal of Geophysical Research* **117**: F02001, doi: 10.1029/2011JF001975.

Buscombe, D., Rubin, D. M. and Warrick, J. A. (2010). A universal approximation of grain size from images of noncohesive sediment, *Journal of Geophysical Research* **115**: F02015. doi:10.1029/2009JF001477.

Butler, J., Lane, S. and Chandler, J. (2001). Automated extraction of grain-size data from gravel surfaces using digital image processing, *Journal of Hydraulic Research* **39**(5): 519–529.

Carbonneau, P. (2005). The threshold effect of image resolution on image-based automated grain size mapping in fluvial environments. *Earth Surface Processes and Landforms*. **30**(13): 1687-1693.

Carbonneau P. Lane, S. and Bergeron N. E. (2004). Catchment-scale mapping of surface grain size in gravel bed rivers using airborne digital imagery, *Water Resources Research*. **40**(W07202).

Carbonneau, P. and Piegay, H. (2012). *Fluvial Remote Sensing for Science and Management*, Chichester, John Wiley and Sons.

Carbonneau, P., Fonstad, M.A., Marcus, W.A., and Dugdale, S. J. (2012). Making riverscapes real, *Geomorphology*, **137**(1): pp. 74-86. doi: 10.1016/j.geomorph.2010.09.030.

Chandler, J. H., Rice, S. and Church, M. (2004). Colour aerial photography for riverbed classification, The International Archives of the Photogrammetry, *Remote Sensing and Spatial Information Sciences*, Vol. **34**(Part XXX), Commission 7, Istanbul, 2004: 1079-1085.
Online via:
http://www.isprs.org/proceedings/XXXV/congress/comm7/papers/206.pdf

Chang, F. and Chung, C. (2012). Estimation of riverbed grain-size distribution using image-processing techniques, *Journal of Hydrology* **440-441**: 102 – 112.

Church, M., McLean, D. and Wolcott, J. (1987). River bed gravels: sampling and analysis, in C. Thorne, J. Bathurst and R. Hey (eds), *Sediment transport in gravel-bed rivers*, Chichester, J. Wiley and Sons (Wiley-Interscience).

Clausi, D. A. (2002). An analysis of co-occurrence texture statistics as a function of grey level quantization, *Canadian Journal of Remote Sensing* **28**(1): 45–62.

Fausch, K. D., Torgersen, C. E., Baxter, C. V., & Li, H. W. (2002). Landscapes to Riverscapes: Bridging the Gap between Research and Conservation of Stream Fishes: A continuous view of the river is needed to understand how process interacting among scales set the context for stream fishes and their habitat. *BioScience*, **52**(6), 483-498.

Friedman, J., Hastie, T. and Tibshirani, R. (2001). *The elements of statistical learning, Vol. 1*, Springer Series in Statistics.

Gonzalez, R. and Woods, R. (2008). *Digital image processing*, Pearson/Prentice Hall.

Graham, D., Reid, I. and Rice, S. (2005a). Automated sizing of coarse-grained sediments: image-processing procedures, *Mathematical Geology* **37**(1): 1–28.

Graham, D., Reid, I. and Rice, S. (2005b). A transferable method for the automated grain sizing of river gravels, *Water Resources Research* **41**: W07020. doi:10.1029/2004WR003868.

Haralick, R. M. (1979). Statistical and structural approaches to texture, *Proceedings of the Institute of Electrical and Electronics Engineers* **67**(5): 786 – 804.

Haralick, R. M., Shanmugam, K. and Dinstein, I. (1973). Textural features for image classification, *Systems, Man and Cybernetics, Institute of Electrical and Electronics Engineers Transactions on* **3**(6): 610 –621.

Ham, D. (2005). *Morphodynamics and sediment transport in a wandering gravel-bed channel: Fraser River, British Columbia*, PhD thesis, Department of Geography, University of British Columbia, Canada. Online via: http://www.geog.ubc.ca/fraserriver/reports/morphodynamics.pdf [60 Mb].

Ham, D. and Church, M. (2003). *The sediment budget in the gravel reach of the Fraser River: 2003 revision*, Department of Geography, University of British Columbia. Online via: http://www.geog.ubc.ca/fraserriver/reports/sedbudget2003rev4.pdf: [0.8 Mb].

Ibbeken, H. and Schleyer, R. (1986). Photo-sieving: A method for grain-size analysis of coarse-grained, unconsolidated bedding surfaces, *Earth Surface Processes and Landforms* **11**(1): 59–77.

Klingeman, P. C. (1998). Gravel Bed Rivers in the Environment. *Water Resources Publication*, 832 pp.

Klug W, Graziani G, Grippa G, Pierce D, Tassone C (eds) (1992). *Evaluation of long range atmospheric transport models using environmental radioactivity data from the Chernobyl accident: the ATMES Report.* Elsevier, London, 366 pages

Lane, E. and Carlson, E. (1953). Some factors affecting the stability of canals constructed in coarse granular materials, *Proceedings: Minnesota International Hydraulic Convention, ASCE*, pp. 37–48.

Marcus, W. A. and Fonstad, M. A. (2008). Optical remote mapping of rivers at sub-meter resolutions and watershed extents, *Earth Surface Processes and Landforms* **33**(1): 4–24.

McEwan, I., Sheen, T., Cunningham, G. and Allen, A. (2000). Estimating the size composition of sediment surfaces through image analysis, *Proceedings of the Institution of Civil Engineers. Water, maritime and energy* **142**(4): 189–195.

Otsu, N., (1979). A Threshold Selection Method from Gray-Level Histograms, *IEEE Transactions on Systems, Man, and Cybernetics*, **9**(1), pp. 62-66.

Perica, S and Foufoula-Georgiou, E. (1996). Model for multiscale disaggregation of spatial rainfall based on coupling meteorological and scaling descriptions. *Journal of Geophysical Research: Atmospheres* **101**(D21), pp. 26347–26361 DOI: 10.1029/96JD01870

Pina, P., Lira, C. and Lousda, M. (2011). In-situ computation of granulometries of sedimentary grains - some preliminary results, *Journal of Coastal Research*, Special Edition **64**, pp. 1727–1730.

Pontius, R., Boersma, W., Castella, J., Clarke, K., de Nijs, T., Dietzel, C., Duan, Z., Fotsing, E., Goldstein, N., Kok, K. et al. (2008). Comparing the input, output, and validation maps for several models of land change, *The Annals of Regional Science* **42**(1): 11–37.

Rango, A., Laliberte, A., Herrick, J. E., Winters, C., Havstad, K., Steele, C. and Browning, D. (2009). Unmanned aerial vehicle-based remote sensing for rangeland assessment, monitoring, and management, *Journal of Applied Remote Sensing* **3**(1): 033542–033542–15.

Rosenau, M. L. and Angelo, M. (2007). *Saving the Heart of the Fraser: Addressing Human Impacts to the Aquatic Ecosystem of the Fraser River, Hope to Mission, BC*. Pacific Fisheries Resource Conservation Council.

Rubin, D. M. (2004). A simple autocorrelation algorithm for determining grain size from digital images of sediment, *Journal of Sedimentary Research* **74**(1): 160–165.

Soh, L.-K. and Tsatsoulis, C. (1999). Texture analysis of sar sea ice imagery using gray level co-occurrence matrices, *Geoscience and Remote Sensing, Institute of Electrical and Electronics Engineers Transactions on* **37**(2): 780 –795.

Verdu, J. M., Batalla, R. J. and Martinez-Casasnovas, J. A. (2005). High-resolution grain-size characterisation of gravel bars using imagery analysis and geo-statistics, *Geomorphology* **72**(1-4): 73 – 93.

FIGURE CAPTIONS

Figure 1: Location map showing the areas of hyperspatial image acquisition (red boxes) and four study bar locations.

Figure 2: An example of a calibration site prepared for the 'paint and pick' technique used to collect ground truth grain-size data. Gradations on the frame are 10 cm apart.

Figure 3: Shows the collage image composed of three distinct images (A) and the manual delineation results overlain on the image (B), where non-sand areas delineated are shown in beige. The two irregular features present in the middle frame are patches of wood.

Figure 4: An example of calculating a Grey Level Co-occurrence Matrix (adapted from Gonzalez and Woods, 2008).

Figure 5: Flow chart showing the workflow for deriving grain-size maps.

Figure 6: All 23 measured grain-size distributions from Fraser River Bar sites.

Figure 7: Change in FoM accuracy with increasing window size and a fixed threshold value of 3.5.

Figure 8: Change in FoM accuracy with a fixed window size of 3 x 3 and increasing threshold values.

Figure 9: Change in r2 statistic with increasing window size for D50.

Figure 10: Change in r2 statistic with increasing window size for D95.

Figure 11: Average r2 values per percentile over the 'top 1000' parameter sets.

Figure 12: Frequency of 16 grey levels averaged over the 'top 1000' parameter sets.

Figure 13: Variation in r2 for the combinations of parameters: (A) offset (x) and offset (y); (B) offset (x) and window size; and (C) offset (y) and window size. The fixed parameters given in the title of each graph represent the best parameter set (Table 4).

Figure 14: Observed versus predicted grain size for each of the reference percentiles.

Figure 15: N Bar: Hyperspatial imagery of the bar (A) and D50 grain-size map (B).

Figure 16: (A) Composite image. (B) to (E) Classifications at increasing threshold values calculated from the green band of the composite image, where grey represents sand.

Figure 17: Visual depiction of the differing image texture measures with increasing spatial resolution for a sample grain-size percentile, Dn. Point μ represents the point at which the grain size of sample Dn and the spatial resolution are equal.

Window Size	GLCM Statistic	Offset (x)	Offset (y)	Grey Levels	Band
3 x 3	**Contrast**	**0**	**0**	**16**	**R**
5 x 5	**Correlation**	**1**	**1**	**32**	**G**
...	**Entropy**	**...**	**...**	**64**	**B**
69 x 69		**8**	**8**		**NIR**

	Minimum	Maximum	Range	Mean
D_5	**1.52**	**2.04**	**0.52**	**1.64**
D_{16}	**1.75**	**2.89**	**1.14**	**2.12**
D_{35}	**2.24**	**4.41**	**2.17**	**3.08**
D_{50}	**2.73**	**5.89**	**3.16**	**4.15**
D_{65}	**3.62**	**8.44**	**4.82**	**5.83**
D_{84}	**6.58**	**13.40**	**6.82**	**10.35**
D_{95}	**15.23**	**23.41**	**8.18**	**19.26**

	W	B	r^2	MSE (mm)
D_5	**55**	**4**	**0.62**	**0.01**
D_{16}	**55**	**4**	**0.68**	**0.04**
D_{35}	**57**	**4**	**0.66**	**0.16**

D_{50}	**55**	**4**	**0.63**	**0.39**
D_{65}	**25**	**4**	**0.58**	**0.88**
D_{84}	**25**	**2**	**0.36**	**2.54**
D_{95}	**3**	**4**	**0.12**	**5.15**

		Ox	Oy	W	B	GL	r^2	MSEcv (mm)	MSEcv (%)	Relative Error (%)
CONTRAST	D_5	**4**	**0**	**59**	**2**	**16**	**0.67**	**0.02**	**1.28**	**4.03**
	D_{16}	**5**	**0**	**61**	**2**	**16**	**0.73**	**0.06**	**2.61**	**4.86**
	D_{35}	**5**	**0**	**51**	**2**	**16**	**0.75**	**0.30**	**9.77**	**13.87**
	D_{50}	**5**	**0**	**51**	**2**	**16**	**0.75**	**0.64**	**15.40**	**20.22**
	D_{65}	**5**	**0**	**51**	**2**	**16**	**0.71**	**1.26**	**21.67**	**26.21**
	D_{84}	**6**	**0**	**51**	**2**	**16**	**0.45**	**3.15**	**30.46**	**46.22**
	D_{95}	**1**	**0**	**17**	**3**	**16**	**0.28**	**6.37**	**33.05**	**77.82**
CORRELATION	D_5	**0**	**1**	**51**	**4**	**16**	**0.73**	**0.01**	**0.67**	**2.12**
	D_{16}	**0**	**1**	**49**	**4**	**16**	**0.72**	**0.05**	**2.33**	**4.33**
	D_{35}	**0**	**1**	**41**	**4**	**16**	**0.71**	**0.43**	**14.10**	**20.01**
	D_{50}	**0**	**1**	**21**	**4**	**16**	**0.67**	**0.60**	**14.44**	**18.97**
	D_{65}	**0**	**1**	**21**	**4**	**16**	**0.64**	**1.37**	**23.48**	**28.40**
	D_{84}	**4**	**2**	**23**	**3**	**16**	**0.59**	**3.02**	**29.15**	**44.24**
	D_{95}	**2**	**4**	**41**	**4**	**16**	**0.51**	**6.83**	**35.45**	**83.48**
ENTROPY	D_5	**2**	**7**	**69**	**2**	**16**	**0.71**	**0.01**	**0.55**	**1.720**
	D_{16}	**1**	**3**	**21**	**2**	**16**	**0.72**	**0.05**	**2.59**	**4.808**
	D_{35}	**1**	**3**	**21**	**2**	**16**	**0.70**	**0.23**	**7.54**	**10.697**
	D_{50}	**1**	**3**	**21**	**2**	**16**	**0.65**	**0.56**	**13.47**	**17.695**
	D_{65}	**1**	**3**	**21**	**2**	**16**	**0.57**	**1.31**	**22.45**	**27.150**
	D_{84}	**2**	**5**	**23**	**2**	**16**	**0.29**	**4.42**	**42.73**	**64.849**
	D_{95}	**5**	**8**	**17**	**3**	**64**	**0.44**	**5.36**	**27.82**	**65.501**

	C	S	C_N	C_R	E	MSEcv (mm)	MSEcv (%)	Relative Error (%)
D_5	**2.89**	**0.01**	**-0.02**	**-1.23**	**-0.27**	**0.01**	**0.46**	**1.44**
D_{16}	**4.69**	**0.05**	**-0.30**	**-2.33**	**-0.60**	**0.04**	**1.71**	**3.18**

D_{35}	7.63	0.20	-0.91	-4.47	-1.43	0.15	4.79	6.80
D_{50}	8.57	0.23	-2.07	-4.83	-1.11	0.33	8.04	10.56
D_{65}	10.50	-0.01	-2.85	-6.23	0.87	0.83	14.23	17.21
D_{84}	6.98	-0.01	-4.52	43.11	2.47	1.69	16.29	24.73
D_{95}	8.15	0.12	-4.77	-33.02	3.65	2.43	12.62	29.71

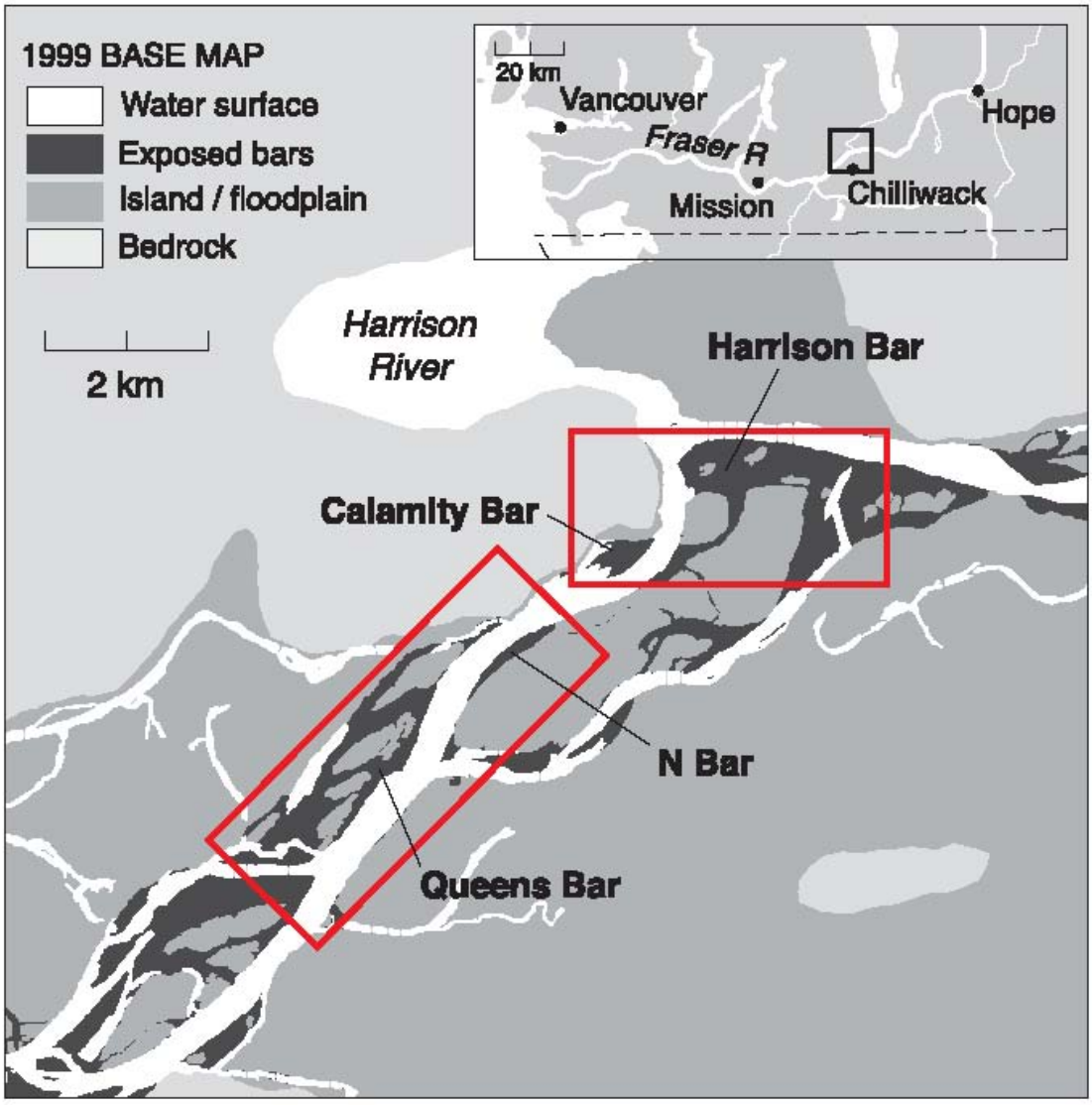

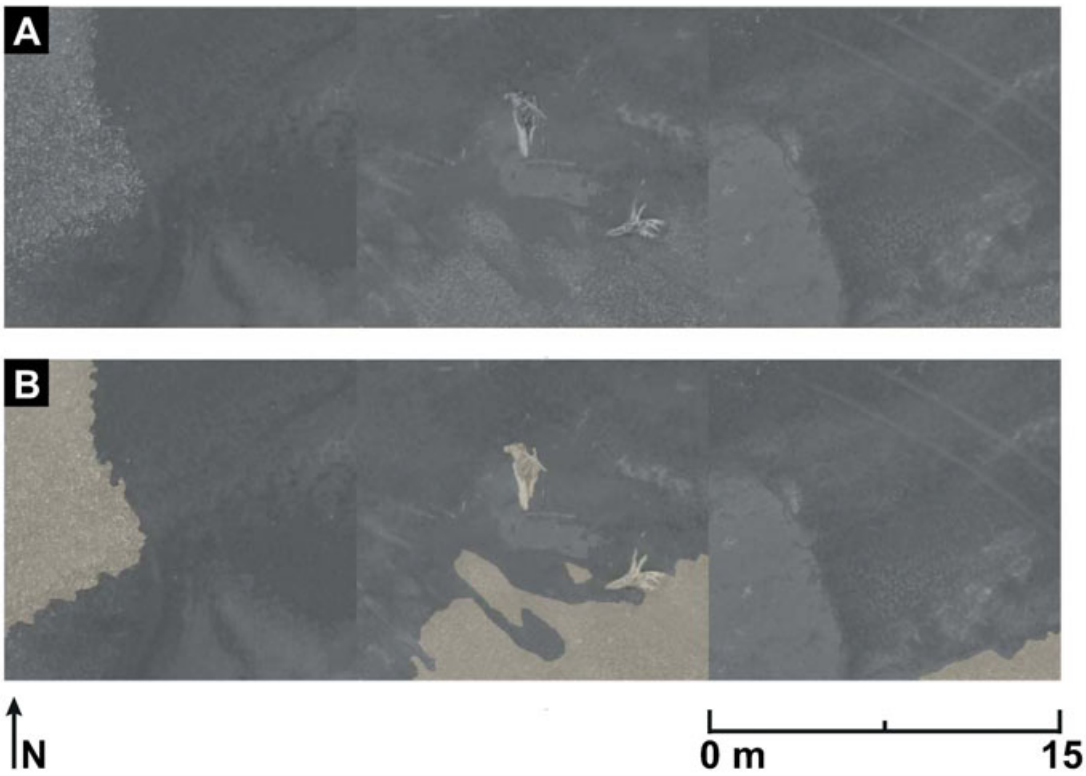

1	1	7	5	3	2
5	1	6	1	2	5
8	8	6	8	1	2
4	3	4	5	5	1
8	7	8	7	6	2
7	8	6	2	6	2

Image, *f*

	1	2	3	4	5	6	7	8
1	1	2	0	0	0	1	1	0
2	0	0	0	0	1	1	0	0
3	0	1	0	1	0	0	0	0
4	0	0	1	0	1	0	0	0
5	2	0	1	0	1	0	0	0
6	1	3	0	0	0	0	0	1
7	0	0	0	0	1	1	0	2
8	1	0	0	0	0	2	2	1

GLCM, **G**